2026 IEEE International Conference on Robotics and Automation (ICRA 2026)
June 1-5, 2026. Vienna, Austria

Motion Pattern Analysis of a Rolling Locomotion Robot Featuring Dual Rimless Wheels and Elastic Connectors

Taiki Sedoguchi and Fumihiko Asano

***Abstract*— Rimless wheel, one of the simplest walking models, has been widely studied as a theoretical framework for bipedal locomotion. This study introduces a dual rimless wheel (DRW) connected by elastic elements for maintaining the body shape and investigates its passive locomotion capability through numerical simulations. Simulation results reveal that as the stiffness of the elastic elements increases, the walking behavior approaches that of a rigid rimless wheel, resulting in higher forward velocity. Conversely, lower stiffness enhances body flexibility and enables the generation of low-speed gaits with remarkably small energy loss. These findings suggest that the DRW may be advantageous in environments where collisions have strong impacts, such as compliant terrains. Furthermore, through comparative simulations with several other models, including the rigid rimless wheel, we demonstrate that the low-stiffness DRW model can generate clearly slower passive locomotion while maintaining a feasible walking region. On the other hand, basic prototype experiment indicates that the low-stiffness DRW model achieves more stable and faster walking than the high-stiffness DRW model in low-angle slopes. While the results do not imply that the DRW is universally optimal, they provide new insights into generating soft and stable gaits and underline the usefulness of tensegrity mechanisms.**

I. INTRODUCTION

Rimless wheel (RW) is the simplest walking locomotion model and has been extensively studied for theoretical analysis of passive dynamic walking and biological walking [1]-[3]. In recent years, its hybrid characteristics between wheels and legs have been exploited for practical tasks such as rough-terrain traversal. Examples include using RWs in place of conventional wheels in mobile robots [4], hybrid wheels that allow mutual transformation between circular wheels and RWs [5]-[7], as well as augmenting them with a reaction wheel or telescopic legs to enable active walking [8], [9].

The rimless wheel inherently loses kinetic energy at each collision. This energy loss not only reduces walking efficiency but also transmits impact forces throughout the robot, potentially affecting both the robot itself and the supporting surface. To address these issues and improve walking efficiency while mitigating impacts, various robot designs incorporating flexible elements have been proposed. Specifically, approaches include using spring-loaded telescopic legs to absorb shocks while generating effective propulsion [10], and employing tensegrity structures in which rigid frames are interconnected with flexible elements to balance overall stiffness and compliance [4], [11], [12]. Compared to the simple rimless wheel model, these approaches are expected to enhance practical walking performance and adaptability to complex environments.

In a previous version of this paper, the rolling locomotion model consisting of two cross-shaped rimless wheels, each with four spokes, interconnected by elastic elements was proposed, and its passive locomotion performance on a slope was analyzed [11]. Although the wheels are not rigidly fixed to each other, their relative offset is maintained by the balance of spring tension. This configuration allows impact forces during collisions to be distributed, which is expected to improve walking performance.

However, our previous studies have been limited to demonstrations of passive locomotion in a restricted class of models, and a sufficiently quantitative evaluation has not yet been provided. In this paper, we extend the analysis of physical parameters by introducing a more general mathematical model. Furthermore, we conduct a comparative study of the DRW with other representative models, the rigid RW and the RW with a wobbling mass, to analyze its walking characteristics and discuss its potential advantages.

II. MODELING

A. Dual Rimless Wheel Model

Fig. 1 shows the mathematical models of DRW. The DRW is a tensegrity robotic system consisting of two rimless wheels with n_s spokes connected by ideal linear springs with elastic constant $k_\mathrm{ten}/(2n_\mathrm{s})$ and natural length $l_\mathrm{n} = d\sqrt{2(1-\cos\frac{\alpha}{2})}$ where α denotes the hip angle of each RW, and the whole body shape is maintained by balance of the tension. In the following, an index $k \in \{1, 2\}$ is used to distinguish between the two RWs.

(x_k, z_k) represent the coordinates of the RW's CoM and θ_k represents its angular position with respect to the vertical axis. Let m and I denote the mass and moment of inertia of the RW, respectively, and the total mass of the robotic system is given by $2m$. Let d be the distance from the CoM of the RW to the attachment points of the springs connecting the two RWs. Let the tips be denoted V_i ($i \in \{1, \cdots, 2n_\mathrm{s}\}$), with their position vectors $\boldsymbol{r}_i := [\ x_i \quad z_i\ ]^\mathrm{T}$.

B. Equation of Motion

The equation of motion for DRW is given by

$$\boldsymbol{M}\ddot{\boldsymbol{q}} + \boldsymbol{h} = \boldsymbol{F} + \boldsymbol{J}^\mathrm{T}\boldsymbol{\lambda}, \tag{1}$$

This research was partially supported by Grant-in-Aid for Scientific Research (C) No. 23K03727 provided by the Japan Society for the Promotion of Science (JSPS), Japan Grant Number JPMJSP2102 provided by Japan Science and Technology Agency (JST), and R&D Grants for FY2024 provided by Azbil Yamatake General Foundation.

The Autors are with the Graduate School of Advanced Science and Technology, Japan Advanced Institute of Science and Technology, 1-1 Asahidai, Nomi, Ishikawa 923-1292, Japan {sedoguchi,fasano}@jaist.ac.jp

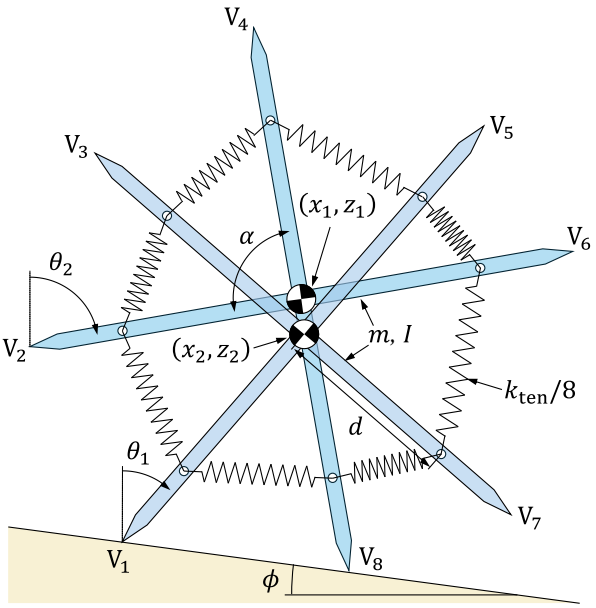

Fig. 1: Mathematical model of the dual rimless wheels robot where $n_{\text{s}} = 4$

where

$$\boldsymbol{q} = \begin{bmatrix} \boldsymbol{q}_1 \\ \boldsymbol{q}_2 \end{bmatrix}, \boldsymbol{M} = \begin{bmatrix} \boldsymbol{M}_1 & \boldsymbol{0}_{3\times3} \\ \boldsymbol{0}_{3\times3} & \boldsymbol{M}_2 \end{bmatrix}, \tag{2}$$

$$\boldsymbol{h} = \begin{bmatrix} \boldsymbol{h}_1 \\ \boldsymbol{h}_2 \end{bmatrix}, \boldsymbol{F} = \begin{bmatrix} \boldsymbol{F}_1 \\ \boldsymbol{F}_2 \end{bmatrix}, \boldsymbol{J}^{\mathrm{T}}\boldsymbol{\lambda} = \begin{bmatrix} \boldsymbol{J}_1^{\mathrm{T}}\boldsymbol{\lambda}_1 \\ \boldsymbol{J}_2^{\mathrm{T}}\boldsymbol{\lambda}_2 \end{bmatrix}. \tag{3}$$

Here, $\boldsymbol{q}_k = [\ x_k \quad z_k \quad \theta_k\ ]^{\mathrm{T}}$ is the generalized coordinate vector, $\boldsymbol{M}_k$ is the inertia matrix, $\boldsymbol{h}_k$ is the nonlinear force vector consists of the Coriolis forces, the centrifugal forces and the gravitational forces, $\boldsymbol{F}_k$ is the tension force and resistive force vector between the two RWs, and $\boldsymbol{J}_k^{\mathrm{T}}\boldsymbol{\lambda}_k$ is the holonomic constraint force vector. When the mass of the elastic elements is ignored, the details of the inertia matrix and the nonlinear vector are defined as follows:

$$\boldsymbol{M}_k = \begin{bmatrix} m & 0 & 0 \\ 0 & m & 0 \\ 0 & 0 & I \end{bmatrix}, \boldsymbol{h}_k = \begin{bmatrix} 0 \\ mg \\ 0 \end{bmatrix}, \tag{4}$$

where g denotes the gravitational acceleration. On the other hand, the spring force vector between the RWs is

$$\begin{aligned} \boldsymbol{F}_1 &= \boldsymbol{T_1} + \boldsymbol{R}_1 \\ &= \begin{bmatrix} k_{\text{ten}}(x_2 - x_1) \\ k_{\text{ten}}(z_2 - z_1) \\ d^2 k_{\text{ten}} \sin(\frac{\alpha}{2}) \sin(\theta_2 - \theta_1 - \frac{\alpha}{2}) \end{bmatrix} + \begin{bmatrix} c_{xz}(\dot{x}_2 - \dot{x}_1) \\ c_{xz}(\dot{z}_2 - \dot{z}_1) \\ c_\theta(\dot{\theta}_2 - \dot{\theta}_1) \end{bmatrix} \\ &= -\boldsymbol{F}_2, \end{aligned} \tag{5}$$

where $\boldsymbol{T}_k$ denotes the tension force vector, $\boldsymbol{R}_k$ denotes the resistive force vector for damping vibrations between the frames, c_{xz} denotes the viscous damping coefficient associated with the relative velocity in the X- and Z-directions, and c_θ denotes the viscous damping coefficient associated with the relative angular velocity. Here, in order to avoid resonance of the tensegrity structure, the damping coefficients are defined as follows:

$$c_{xz} = \sqrt{2mk_{\text{ten}}},\ c_\theta = d\sqrt{mk_{\text{ten}} \sin(\tfrac{\alpha}{2})}. \tag{6}$$

With n denoting the number of contact points and assuming that the tip of the stance-leg is constrained to the ground without slipping, the velocity constraint is expressed in the following form:

$$\boldsymbol{J}\dot{\boldsymbol{q}} = \boldsymbol{0}_{2n\times1}, \tag{7}$$

where $\boldsymbol{J} \in \mathbb{R}^{2n\times3}$ is the Jacobian matrix determined according to the constraints such as $\dot{\boldsymbol{r}}_i = \boldsymbol{0}_{2\times1}$. Let $W = \{w_1, \ldots, w_n\} \subseteq \{1, \cdots, 2n_{\text{s}}\}$ denote the index set of the legs in contact with the ground. Then, $\boldsymbol{J}$ is given by:

$$\boldsymbol{J} = \begin{bmatrix} \boldsymbol{J}_{w_1} \\ \vdots \\ \boldsymbol{J}_{w_n} \end{bmatrix}, \quad \boldsymbol{J}_{w_i} = \frac{\partial \dot{\boldsymbol{r}}_{w_i}}{\partial \dot{\boldsymbol{q}}}. \tag{8}$$

The undetermined multiplier vector $\boldsymbol{\lambda}_k \in \mathbb{R}^{2n}$ represents the constraint force acting at the leg tip and the ground (i.e., the ground reaction force), and can be derived from Eqs. (1) and (7) as follows:

$$\begin{aligned} \boldsymbol{\lambda} &= -\boldsymbol{X}^{-1}\left(\boldsymbol{J}\boldsymbol{M}^{-1}(\boldsymbol{F} - \boldsymbol{h}) - \dot{\boldsymbol{J}}\dot{\boldsymbol{q}}\right) \\ &= \begin{bmatrix} \boldsymbol{\lambda}_{w_1} \\ \vdots \\ \boldsymbol{\lambda}_{w_n} \end{bmatrix}, \end{aligned} \tag{9}$$

where $\boldsymbol{X} := \boldsymbol{J}\boldsymbol{M}^{-1}\boldsymbol{J}^{\mathrm{T}}$, and $\boldsymbol{\lambda}_{w_i} \in \mathbb{R}^2$ represents the ground reaction forces in the X- and Z-directions at each contact point. In the case of no contact points ($n = 0$), $\boldsymbol{J}^{\mathrm{T}}\boldsymbol{\lambda}$ becomes $\boldsymbol{0}_{6\times1}$. Furthermore, if the vertical ground reaction force at a contact point becomes negative, the corresponding constraint is removed, and the generalized accelerations and the ground reaction force vector are recalculated.

C. Equation of Collision

In the numerical simulation, the collision of the legs is determined to occur when the vertical coordinate z_i of the leg tip V_i becomes lower than the ground level, and then $\boldsymbol{J}$ is determined as specified above. Assuming that the collision between the leg tip and the ground is perfectly inelastic, the generalized velocity vector is updated from $\boldsymbol{q}^-$ to $\boldsymbol{q}^+$ according to the following equations.

$$\boldsymbol{M}\dot{\boldsymbol{q}}^+ = \boldsymbol{M}\dot{\boldsymbol{q}}^- + \boldsymbol{J}^{\mathrm{T}}\boldsymbol{\chi}, \tag{10}$$

$$\boldsymbol{J}\dot{\boldsymbol{q}}^+ = \boldsymbol{0}_{2n\times1}, \tag{11}$$

where $\boldsymbol{J}^{\mathrm{T}}\boldsymbol{\chi}$ is the impulse vector at the contact point. Similarly to the derivation of the ground reaction force, if the vertical component of $\boldsymbol{\chi}$ at a contact point becomes negative, the corresponding constraint is released, and the generalized velocities and the impulse vector are recalculated.

III. LOCOMOTION ANALYSIS

Based on the equations derived in the previous section, passive locomotion experiments were conducted through numerical simulations. The physical parameters of DRW and experimental environment are shown in Table I. The integration was performed using the ode45 function in MATLAB with a step size of 10^{-5} sec. In the simulation, forward motion was determined according to the index of the tip of the colliding leg, and walking was regarded a failure if forward progression was not achieved for more than 5 sec. In addition, to prevent unstable switching of contact points, lift-off is determined when the vertical ground reaction force at the leg tip falls below -1×10^{-5} N.

A. Effect of Elastic Coefficient

Fig. 2 shows the average forward velocity along the X-axis for various values of the elastic coefficient of the springs, k_{ten}, and the slope angle, ϕ. The values represent the average over 10 steps after walking 20 steps.

From the figure, it can be seen that the forward velocity increases as k_{ten} and ϕ increase, reaching a peak around $k_{\mathrm{ten}} = 250$ N/m when $\phi = 0.3$ rad. When $\phi = 0.1$ rad, walking failures are observed in the range of $k_{\mathrm{ten}} = 80$–500 N/m. In this parameter region, a double-support phase occurs within a single frame, and the walking fails due to a significant reduction in the rotational velocity. This does not imply that walking is fundamentally infeasible in this region; rather, successful walking may still be achieved depending on the initial conditions. On the other hand, walking is achieved around $k_{\mathrm{ten}} = 70$ N/m under the condition of $\phi = 0.1$ rad. These results clearly indicate that an appropriate level of flexibility can improve locomotion ability and performance.

Figs. 3 and 4 represent the simulation results of typical passive rolling on a slope where $\phi = 0.1$ rad. In each figure, (a) shows the angular velocity of each RW, (b) shows the total mechanical energy, and (c) shows the stick diagram at intervals of 0.2 sec. Here, the total mechanical energy Q is given by

$$Q = U_g + U_e + K \tag{12}$$

where $U_g = mg(z1 + z2 - (x_1 + x_2)\tan\phi)$ denotes the potential energy measured from the ground level, U_e denotes the potential energy stored in the elastic elements, and K denotes the kinetic energy. That is, it represents the mechanical energy neglecting the decrease in potential energy by descending the slope. From Fig. 3 (b), it can be observed that when k_{ten} is small, the variations in mechanical energy are smoothed out, and both the energy recovered during the stance phase and the energy loss at each collision are reduced. Fig. 3 (c) indicates that when the elastic coefficient is small, the oscillation between the frames becomes large and occurs in opposite phase. Most of each step is spent in the double-support phase, and a soft impact of the fore-leg occurs immediately after lift-off of the rear-leg. In contrast, Fig. 4 (c) illustrates that as the elastic coefficient increases, the oscillation decreases and transitions to in-phase vibration.

TABLE I: Physical parameters in simulations

m	1	kg
L	0.5	m
d	0.3	m
I	$mL^2/4$	kg·m^2
n_{L}	4	-
g	9.81	m/s^2
$\theta_1(0)$	ϕ	rad
$\theta_2(0)$	$\phi + \alpha/2$	rad
$\dot{\theta}_1(0) = \dot{\theta}_2(0)$	0.1	rad/s

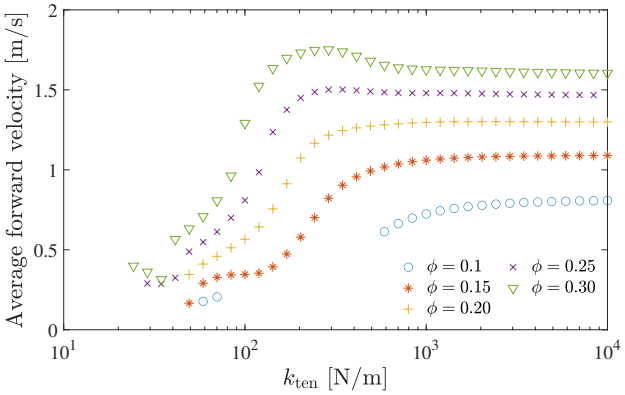

Fig. 2: Average forward velocity vs k_{ten} and ϕ

We can see that most of each step is spent in the single-support phase, and the double-support phase is very short.

B. Effect of Damping Coefficient

In this section, the influence of the damping coefficient on the system is investigated. For the damping coefficients c_{xz} and c_θ given in Eq. (6), a positive constant κ is defined such that $c'_{xz} = \kappa c_{xz}$ and $c'_\theta = \kappa c_\theta$.

Fig. 5 shows the step period of the DRW over 50 steps for various values of κ, where (a) corresponds to $k_{\mathrm{ten}} = 60$ N/m and (b) corresponds to $k_{\mathrm{ten}} = 1000$ N/m. From the figure, it can be seen that as the damping coefficient increases, the step period decreases, meaning that the walking becomes slower. This is considered to be due to the reduction in energy dissipation caused by the damping forces. In Fig. 5 (a), a period-two gait appears at the beginning of walking, which gradually converges to a period-one gait, and it is observed that the convergence becomes faster with increasing damping coefficient. When κ exceeds 1, however, the system becomes overdamped, and the convergence deteriorates. On the other hand, in the DRW with a higher elastic coefficient shown in Fig. 5 (b), no period-two gait is observed, and the step period quickly converges to a constant value within approximately 10 steps. A similar tendency is observed in this model as well, where a decrease in the damping coefficient leads to an increase in walking speed.

C. Comparison with Other Models

To evaluate the superiority of DRW, comparison with other models is indispensable. In this paper, we compare the walking characteristics with two widely studied types of

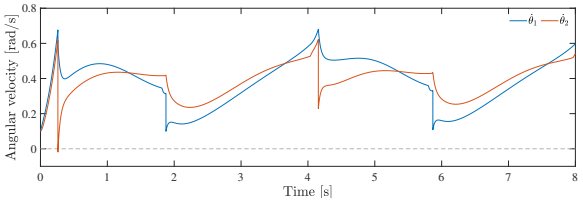

(a) Angular velocity

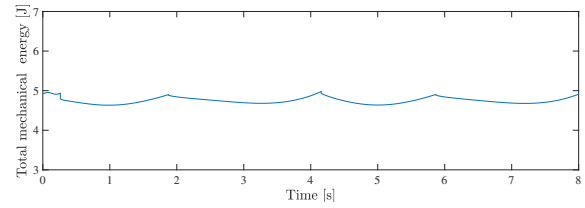

(b) Total mechanical energy

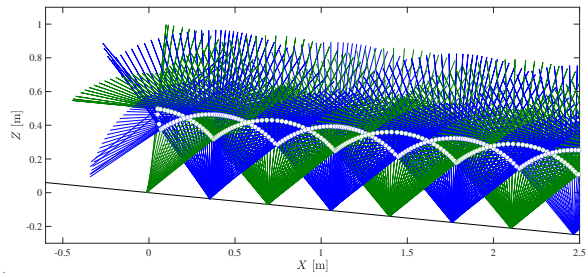

(c) Stick diagram

Fig. 3: Simulation results where $k_{\mathrm{ten}} = 60$ N/m

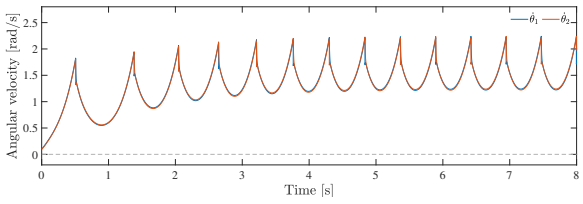

(a) Angular velocity

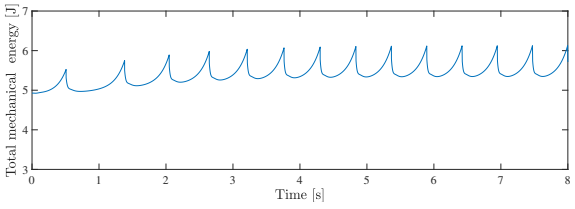

(b) Total mechanical energy

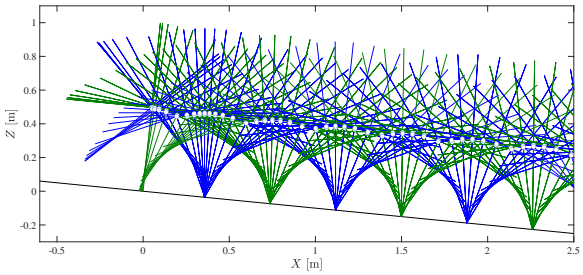

(c) Stick diagram

Fig. 4: Simulation results where $k_{\mathrm{ten}} = 1000$ N/m

rimless wheels: a rigid RW, and an RW with a wobbling mass connected by a viscoelastic element. Moreover, we propose an RW equipped with a wobbling mass connected via a tensegrity structure and include it as a comparison model.

It is known that biological organisms can mitigate impact forces during collisions using wobbling masses composed of soft tissues within their bodies [13]. Similarly, in RW, the addition of an oscillating mass has been shown to reduce energy loss, induce the entrainment phenomenon, and thus improve walking performance [14]-[16].

Hereafter, a wobbling mass connected by a single viscoelastic element is referred to as a SWM (single-spring wobbling mass), whereas a wobbling mass connected via a tensegrity structure is referred to as a TWM (tensegrity wobbling mass), shown in Fig. 6. The RWs with a wobbling mass are modeled with $n_{\mathrm{s}} = 8$ spokes. For the SWM, the wobbling mass is set to $m_{\mathrm{w}} = m = 1, \mathrm{kg}$ and is assumed to have no moment of inertia. For the TWM, the wobbling mass and moment of inertia are set to $m_{\mathrm{w}} = m = 1$ kg and $I_{\mathrm{w}} = I = mL^2/4$ kg·m^2, respectively. On the other hand, the rigid RW is assigned a mass of 2 kg and has $n_{\mathrm{s}} = 8$ spokes. Collisions between the wobbling masses and the ground are not considered in the simulation; however, they often occur when low-stiffness springs are used.

Fig. 7 shows the average forward velocity of each model as a function of the slope angle. From the figure, it can be seen that the soft DRW exhibits lower walking speeds but maintains a wide walkable region. In contrast, the stiff

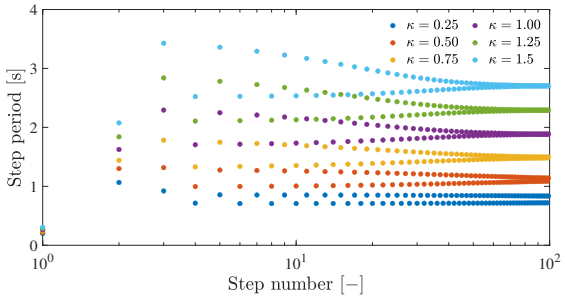

(a) $k_{\mathrm{ten}} = 60$ N/m

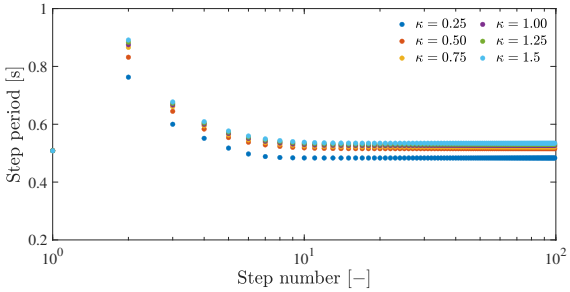

(b) $k_{\mathrm{ten}} = 1000$ N/m

Fig. 5: Step period with various damping coefficient

DRW shows a trend almost identical to that of the rigid RW, although at larger slope angles (greater than 0.35 rad), it achieves higher walking speeds than the RW. For the RW with TWM, models with a small elastic coefficient exhibit

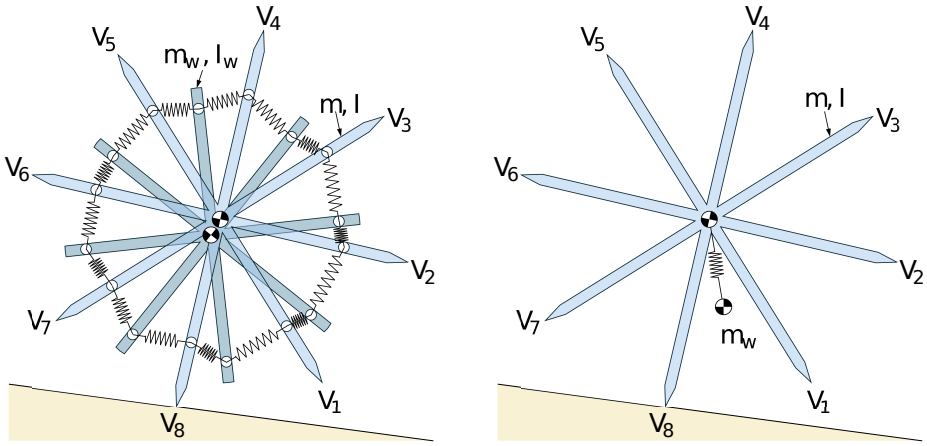

(a) Tensegrity wobbling mass (b) Single-spring wobbling mass

Fig. 6: Rimless wheels with a wobbling mass

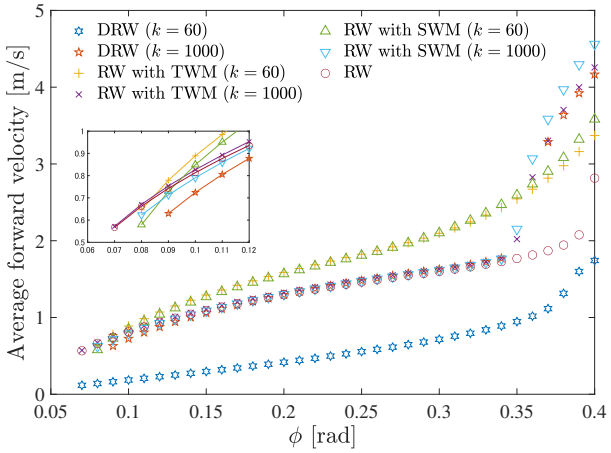

Fig. 7: Average walking speed of each model

relatively high walking speeds at small slope angles, whereas the TWM model with a large elastic coefficient achieves the widest walkable region and is able to move at high speed. Furthermore, when comparing the SWM and TWM models with the high elastic coefficient, it is found that although both exhibit similar trends, the TWM achieves higher walking speeds at small slope angles, while the SWM outperforms at larger slope angles.

Although these results do not indicate that the DRW models are optimal, it provides a new finding that slow and soft gaits can be generated. In addition, the high walking performance of the RW with a TWM suggests the usefulness of tensegrity connections.

IV. EXPERIMENTAL DEMONSTRATION

This section describes the fabrication of the experimental prototype and the passive locomotion experiments. Fig. 8 shows the external appearance of the prototype. The prototype is made of PLA resin and was fabricated using a fused deposition modeling (FDM) 3D printer. The white components connected at the center of each frame are spacers made of the same material, which are used to suppress lateral displacement. Each frame has four legs, and the mass of each frame including the spacer, m, is 180 g (± 5 g). The leg length L is 100 mm, the distance from the frame center to the spring attachment point d is 80 mm, and the leg width in the lateral direction is 100 mm. These frames are connected by tension springs, as in the mathematical model. We used two types of springs (soft and hard) with different physical parameters: the soft spring has a stiffness of 0.014 N/mm and a natural length of 29.9 mm, whereas the hard spring has a stiffness of 0.845 N/mm and a natural length of 30.7 mm.

The experimental setup and representative results are shown in Fig. 9 and the supplementary video. In the experiments, the soft-spring model achieved forward locomotion at 0.250 m/s for a slope angle of 0.056 rad, and at 0.176 m/s for 0.028 rad. However, when the slope angle is further increased, chaotic walking behavior with severe oscillations is observed. In contrast, the hard-spring model exhibited a lower walking speed of 0.196 m/s at 0.056 rad, and failed to walk at 0.028 rad. For this model, more stable walking was achieved as the slope angle increased. These results suggest that the soft-spring DRW is more suitable for locomotion on low-angle slopes, whereas the hard-spring DRW is preferable on high-angle slopes.

One possible reason for the acceleration of soft-spring model on low-angle slopes is that the physical prototype has shorter leg lengths and lower friction between the frames. Since the leg length strongly affects the moment of inertia, the soft-spring model may be capable of generating stable locomotion with reduced sensitivity to the moment of inertia. In addition, lower inter-frame friction reduces the dissipated energy due to relative changes in the CoM position, thereby expanding the stable locomotion region. Furthermore, forward locomotion may also be excited by chaotic behavior and basin-of-attraction effects. The assumptions made for collision modeling in the simulations may also have influenced the analysis results. A more detailed analysis is required in future work.

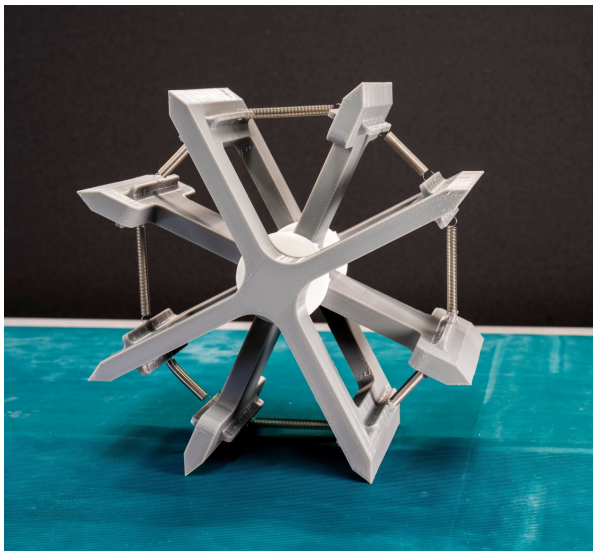

Fig. 8: Appearance of prototype

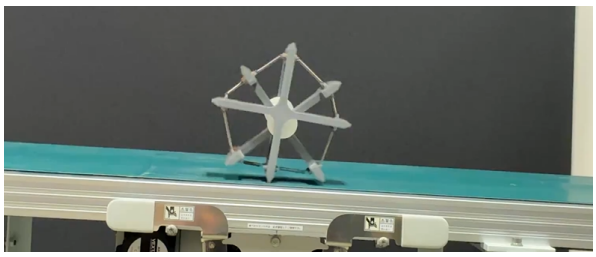

Fig. 9: Passive locomotion experiment

V. CONCLUSIONS

In this study, we derived the mathematical model of the dual rimless wheels (DRW) robotic system connected by elastic elements and investigated its effectiveness through passive locomotion experiments. The proposed model has a very simple mathematical formulation and is novel in that the body shape is maintained solely by the balance of spring tension.

Numerical simulations demonstrated that as the elastic coefficient increases, the behavior becomes closer to that of a rigid RW and the walking speed increases. Conversely, when the elastic coefficient decreases, the body flexibility raises, enabling the generation of a low-speed gait with extremely small energy loss. These results suggest that the proposed model may be particularly useful in environments where the effects of collisions are pronounced, such as on compliant surface or deformable terrain.

Additionally, the experimental results demonstrated that the prototype of the soft-spring DRW achieved more stable and faster walking than the hard-spring DRW on low-angle slopes. In contrast, on high-angle slopes, the hard-spring DRW exhibited more stable gait patterns, suggesting that selecting appropriate stiffness according to the environment is important.

Future work will include detailed motion analyses considering resonance and chaotic behavior under varying damping properties, as well as adaptability to uneven terrain. Furthermore, the proposed framework is expected to enable the development of walking robots with variable flexibility by controlling the joint locations of the springs or their stiffness coefficients.

ACKNOWLEDGMENT

This research was partially supported by Grant-in-Aid for Scientific Research (C) No. 23K03727 provided by the Japan Society for the Promotion of Science (JSPS), JST SPRING; Japan Grant Number JPMJSP2102 provided by Japan Science and Technology Agency (JST), and Research and Development Grants for FY2024 provided by Azbil Yamatake General Foundation.

REFERENCES

[1] T. McGeer, "Passive dynamic walking," *Int. J. of Robotics Research*, vol. 9, no. 2, pp. 62–82, 1990.

[2] M. J. Coleman, A. Chatterjee and A. Ruina, "Motions of a rimless spoked wheel: a simple three-dimensional system with impacts," *Dynamics and Stability of Systems*, vol. 12, no. 3, pp. 139–159, 1997.

[3] F. Asano, "Stability principle underlying passive dynamic walking of rimless wheel," *Proc. of IEEE Int. Conf. on Control Applications*, pp. 1039–1044, 2012.

[4] Y. Xiang, Y. Zheng and F. Asano, "Modeling and analysis of combined rimless wheel with tensegrity spine," *Proc. of IEEE Int. Conf. on Robotics and Automation*, pp. 8088–8093, 2024.

[5] Y. S. Kim, G. P. Jung, H. Kim, K. J. Cho and C. N. Chu, "Wheel transformer: a wheel-leg hybrid robot with passive transformable wheels," *IEEE Trans. on Robotics*, vol. 30, no. 6, pp. 1487–1498, 2014.

[6] Z. Fu, H. Xu, Y. Li and W. Guo, "Design of a novel wheel-legged robot with rim shape changeable wheels," *Chinese J. of Mechanical Engineering*, vol. 36, pp. 153, 2023.

[7] J. Lee, J. Park and Y. Kim, "Torque reduction of 1-DOF transformable wheel with passive springs," *IEEE Access*, vol. 13, pp. 135822–135833, 2025.

[8] Y. Hanazawa, Y. Uchino and S. Sagara, "Development of a rimless wheel robot with telescopic legs for step adaptability," *Artificial Life and Robotics*, vol. 29, pp. 349–357, 2024.

[9] F. Asano and J. Kawamoto, "Passive dynamic walking of viscoelastic-legged rimless wheel," *Proc. of IEEE Int. Conf. Robotics and Automation*, pp. 2331–2336, 2012.

[10] S. Sanchez and P. A. Bhounsule, "Design, modeling, and control of a differential drive rimless wheel that can move straight and turn," *Automation*, vol. 2, no. 3, pp. 98–115, 2021.

[11] F. Asano, Y. Xiang, Y. Zheng and C. Yan, "Motion analysis of planar passive-dynamic walkers with different tensegrity structures formed by four rigid frames and eight viscoelastic elements," *Proc. of Int. Conf. on Advanced Robotics and Mechatronics*, pp. 95–100, 2022.

[12] Y. Zheng, F. Asano, C. Yan, L. Li and I. T. Tokuda, "Tensegrity-based legged robot generates passive walking, skipping, and crawling gaits in accordance with environment," *IEEE/ASME Trans. on Mechatronics*, vol. 30, no. 6, pp. 6361–6372, 2025.

[13] S. Schmitt and M. Günther, "Human leg impact: energy dissipation of wobbling masses," *Archives of Applied Mechanics*, vol. 81, pp. 887–897, 2011.

[14] D. Tanaka, F. Asano and I. T. Tokuda, "Gait analysis and efficiency improvement of passive dynamic walking of combined rimless wheel with wobbling mass," *Proc. of IEEE/RSJ Int. Conf. Intelligent Robots and Systems*, pp. 151–156, 2012.

[15] F. Asano, T. Sogawa, K. Tamura and Y. Akutsu, "Passive dynamic walking of rimless wheel with 2-DOF wobbling mass," *Proc. of IEEE/RSJ Int. Conf. Intelligent Robots and Systems*, pp. 3120–3125, 2013.

[16] Y. Hanazawa, "Development of rimless wheel with controlled wobbling mass," *Proc. of IEEE/RSJ Int. Conf. on Intelligent Robots and Systems*, pp. 4333–4339, 2018.